

# High angular resolution $N$ -band observation of the silicate carbon star IRAS08002-3803 with the VLT/MIDI instrument $\star$

## Dusty environment spatially resolved

K. Ohnaka<sup>1</sup>, T. Driebe<sup>1</sup>, K.-H. Hofmann<sup>1</sup>, Ch. Leinert<sup>2</sup>, S. Morel<sup>3</sup>, F. Paresce<sup>4</sup>, Th. Preibisch<sup>1</sup>, A. Richichi<sup>4</sup>, D. Schertl<sup>1</sup>, M. Schöller<sup>3</sup>, L. B. F. M. Waters<sup>5</sup>, G. Weigelt<sup>1</sup>, M. Wittkowski<sup>4</sup>

<sup>1</sup> Max-Planck-Institut für Radioastronomie, Auf dem Hügel 69, 53121 Bonn, Germany  
e-mail: kohnaka@mpi.fr-bonn.mpg.de

<sup>2</sup> Max-Planck-Institut für Astronomie, Königstuhl 17, 69117 Heidelberg, Germany

<sup>3</sup> European Southern Observatory, Casilla 19001, Santiago 19, Chile

<sup>4</sup> European Southern Observatory, Karl-Schwarzschild-Str. 2, 85748 Garching, Germany

<sup>5</sup> Astronomical Institute “Anton Pannekoek”, Kruislaan 403, 1098 SJ Amsterdam, The Netherlands

Received / Accepted

**Abstract.** We present the results of  $N$ -band spectro-interferometric observations of the silicate carbon star IRAS08002-3803 with the MID-infrared Interferometric instrument (MIDI) at the Very Large Telescope Interferometer (VLTI) of the European Southern Observatory (ESO). The observations were carried out using two unit telescopes (UT2 and UT3) with projected baseline lengths ranging from 39 to 47 m. Our observations of IRAS08002-3803 have spatially resolved the dusty environment of a silicate carbon star for the first time and revealed an unexpected wavelength dependence of the angular size in the  $N$  band: the uniform-disk diameter is found to be constant and  $\sim 36$  mas ( $72 R_\star$ ) between 8 and  $10 \mu\text{m}$ , while it steeply increases longward of  $10 \mu\text{m}$  to reach  $\sim 53$  mas ( $106 R_\star$ ) at  $13 \mu\text{m}$ . Model calculations with our Monte Carlo radiative transfer code show that neither spherical shell models nor axisymmetric disk models consisting of silicate grains alone can simultaneously explain the observed wavelength dependence of the visibility and the spectral energy distribution (SED). We propose that the circumstellar environment of IRAS08002-3803 may consist of two grain species coexisting in the disk: silicate and a second grain species, for which we consider amorphous carbon, large silicate grains, and metallic iron grains. Comparison of the observed visibilities and SED with our models shows that such disk models can fairly — though not entirely satisfactorily — reproduce the observed SED and  $N$ -band visibilities. Our MIDI observations and the radiative transfer calculations lend support to the picture where oxygen-rich material around IRAS08002-3803 is stored in a circumbinary disk surrounding the carbon-rich primary star and its putative low-luminosity companion.

**Key words.** infrared: stars – techniques: interferometric – stars: circumstellar matter – stars: carbon – stars: AGB and post-AGB – stars: individual: IRAS08002-3803

## 1. Introduction

Slow but massive mass loss at the asymptotic giant branch (AGB) leads to the formation of circumstellar dust envelopes. The dust species formed in the circumstellar envelope reflect the chemical composition of the photosphere, that is, dust grains such as silicate and corundum ( $\text{Al}_2\text{O}_3$ ) are observed around oxygen-rich stars (M giants), while amorphous carbon and/or silicon carbide (SiC) are observed around carbon stars.

Therefore, the discovery of carbon stars showing (amorphous) silicate emission in the IRAS Low Resolution Spectra

*Send offprint requests to:* K. Ohnaka

$\star$  Based on observations made with the Very Large Telescope Interferometer of the European Southern Observatory. Program ID: 073.A-9002(A)

(LRS) by Little-Marennin (1986) and Willems & de Jong (1986) struck stellar spectroscopists as baffling, and the origin of these “silicate carbon stars” is still a puzzle to date. The spectroscopic studies which followed this discovery revealed that the optical and near-infrared spectra of silicate carbon stars are dominated by strong absorption due to  $\text{C}_2$  and CN, confirming that the photospheres of the silicate carbon stars are indeed carbon-rich and they can be classified as J-type carbon stars, which are enriched in  $^{13}\text{C}$  (e.g., Lloyd-Evans 1990; Skinner et al. 1990; Chan 1993). In fact, quantitative spectral analyses show that these silicate carbon stars have  $^{12}\text{C}/^{13}\text{C}$  ratios as low as 4–5 (e.g., Ohnaka & Tsuji 1999; Abia & Isern 2000), which poses a great challenge for stellar evolution theory. On the other hand, detection of  $\text{H}_2\text{O}$  and OH maser emission toward silicate carbon stars confirmed that they are associated

with oxygen-rich circumstellar material (e.g., Nakada et al. 1987, 1988; Benson & Little-Marenin 1987; Little-Marenin et al. 1988; Barnbaum et al. 1991; Engels 1994).

Willems & de Jong (1986) and Chan & Kwok (1991) suggested that silicate carbon stars are objects in transition from M giants to carbon stars. However, this scenario is deemed to be unlikely as Lloyd-Evans (1990) argues: the time scale for such a transitional object to be observed as a silicate carbon star is predicted to be a few decades, while some of the silicate carbon stars are known to have carbon-rich photospheres for 50 years (Little-Marenin et al. 1987). Furthermore, the infrared spectrum of the silicate carbon star V778 Cyg observed by Yamamura et al. (2000) with the Infrared Space Observatory (ISO) reveals that the silicate features at 10 and 18  $\mu\text{m}$  exhibit no temporal variation 14 years after IRAS LRS, which makes it unlikely that silicate carbon stars are short-lived transitional objects. Little-Marenin (1986) proposed that silicate carbon stars are binaries consisting of a carbon star and an M giant, but this scenario has now also been rejected, because near-infrared spectroscopy (Lambert et al. 1990) as well as near-infrared speckle interferometry (Engels & Leinert 1994) detected no hint of an M giant companion toward silicate carbon stars.

At the moment, the most widely accepted hypothesis suggests that silicate carbon stars have a low-luminosity companion (instead of an M giant companion), and that oxygen-rich material was shed by mass loss when the primary star was an M giant and this oxygen-rich material is stored in a circumbinary disk (Morris 1987; Lloyd-Evans 1990) or in a circumstellar disk around the companion (Yamamura et al. 2000) until the primary star becomes a carbon star. In fact, there is observational evidence of binarity and the presence of such a disk for some—if not all—silicate carbon stars. Lloyd-Evans (1990) argues against the shell geometry based on the extinction in the optical as well as in the near-infrared and the amount of the far-infrared excesses found in some silicate carbon stars (including IRAS08002-3803 studied here). Radial velocity measurements of two silicate carbon stars by Barnbaum (1991) are consistent with motion in a binary system. Evidence for the presence of a low-luminosity companion surrounded by an accretion disk was found in the violet spectrum of the silicate carbon star BM Gem (Izumiura 2003). The presence of long-lived reservoirs of orbiting gas is inferred from the narrow CO emission lines ( $J = 1 - 0$  and  $J = 2 - 1$ ) obtained by Kahane et al. (1998) and Jura et al. (1999). Recent high-resolution 22 GHz  $\text{H}_2\text{O}$  maser maps toward V778 Cyg obtained by Szczerba et al. (2005) and Engels (priv. comm.) also suggest the existence of a rotating disk.

However, the geometry of the reservoir of oxygen-rich material is still controversial. Based on the ISO spectrum of V778 Cyg, Yamamura et al. (2000) argue that the oxygen-rich dust is stored in a circumstellar disk around the companion. On the other hand, Molster et al. (1999, 2001) identified pronounced crystalline silicate emission in the silicate carbon star IRAS09425-6040 observed with ISO and postulate that crystalline silicate dust forms in a dense, circumbinary disk. Thus, it is not yet clear whether or not only one of the above two scenarios—circumbinary or circum-companion disk—applies to all silicate carbon stars.

**Table 1.** Summary of the MIDI observations of IRAS08002: date, modified Julian Date (MJD), time of observation (Universal Time=UTC), projected baseline length  $B_p$ , and position angle of the projected baseline on the sky (P.A.).

#	Date	MJD	$t_{\text{obs}}$ (UTC)	$B_p$ (m)	P.A. ( $^\circ$ )
1	2004 Feb. 09	53045.135	03:15:02	46.05	39.48
2	2004 Feb. 09	53045.248	05:56:56	39.11	56.96
3	2004 Feb. 10	53046.137	03:17:44	45.94	40.35
4	2004 Feb. 11	53047.093	02:13:32	46.58	32.03

Observations with high spatial resolution within the silicate emission feature would be a most direct approach for investigating the dusty environment of silicate carbon stars. The MIDI instrument at the VLTI provides us with an excellent opportunity to directly study the circumstellar environment of silicate carbon stars in the 10  $\mu\text{m}$  region, exactly where silicate emission from the oxygen-rich reservoir is located.

In this paper, we present the results of  $N$ -band spectro-interferometric observations of the silicate carbon star IRAS08002-3803 (Hen 38, GCCCS 1003<sup>1</sup>, GCCGS 2011<sup>2</sup>, hereafter IRAS08002), using the VLTI/MIDI instrument. The IRAS LRS of IRAS08002 shows the prominent silicate emission features at 10  $\mu\text{m}$  as well as at  $\sim 18$   $\mu\text{m}$  with a 12  $\mu\text{m}$  flux of 40.3 Jy. While most of the well studied silicate carbon stars are in the northern sky, IRAS08002 is the brightest one among the few silicate carbon stars observable from the VLTI. Lloyd-Evans (1990) notes that IRAS08002 shows a 10  $\mu\text{m}$  feature much broader than that observed in silicate carbon stars such as V778 Cyg and BM Gem. Kwok & Chan (1993) also mention that some silicate carbon stars (including IRAS08002) show silicate emission features broader than usual oxygen-rich AGB stars, while others show silicate features as narrow as in usual AGB stars. No  $\text{H}_2\text{O}$  maser is detected toward IRAS08002 (Nakada et al. 1988; Deguchi et al. 1989), and no radial velocity monitoring observations to confirm its binary nature are available in the literature.

In Sect. 2, we present the observational results. In Sect. 3, we describe our radiative transfer code based on the Monte Carlo technique. The results of our model calculations for IRAS08002 and the comparison with the observations are presented in Sect. 4 and 5. We discuss possible scenarios for the circumstellar environment of IRAS08002 in Sect. 6.

## 2. MIDI observations

IRAS08002 was observed with MIDI on 2004 February 9, 10, and 11 as part of the Science Demonstration Time program. A prism with a spectral resolution of  $\lambda/\Delta\lambda \approx 30$  at 10  $\mu\text{m}$  was used to obtain spectrally dispersed fringes between 8 and 13  $\mu\text{m}$ . A detailed description of the observing procedure is given in Przygodda et al. (2003), Leinert et al. (2004), and Chesneau et al. (2005a, 2005b). Four data sets were obtained

<sup>1</sup> A General Catalogue of Cool Carbon Stars, Stephenson (1973)

<sup>2</sup> A General Catalogue of Cool Galactic Carbon Stars, Stephenson (1989)

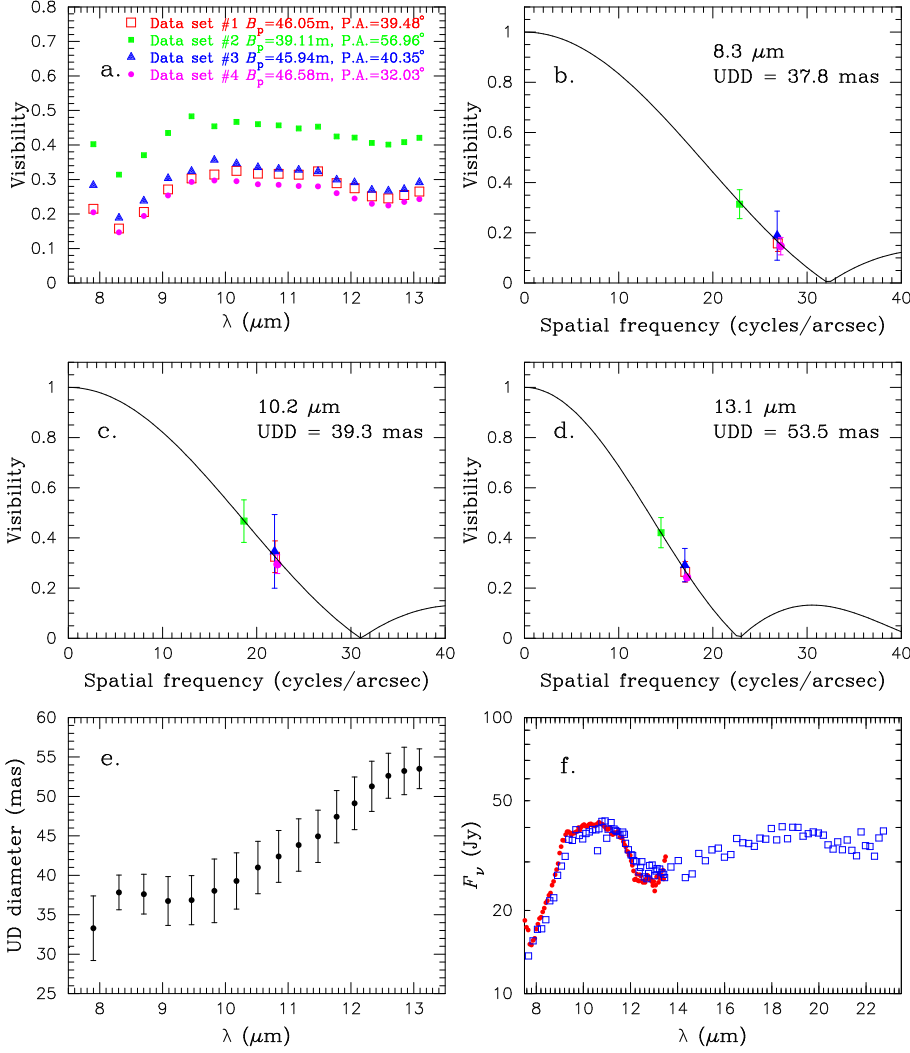


**Fig. 1.**  $N$ -band visibilities and spectra observed for IRAS08002. **a:** Observed visibilities plotted as a function of wavelength. The errors of the observed visibilities are typically  $\pm 10$ –15%, but the error bars are omitted in this panel for the sake of visual clarity. **b–d:** Visibilities at three representative wavelengths in the  $N$  band are plotted as a function of spatial frequency, together with uniform-disk fits. **e:** Uniform-disk diameter (UDD) obtained by fitting the visibility points of all four data sets is plotted as a function of wavelength. **f:** Observed spectra of IRAS08002. The absolutely calibrated MIDI spectrum is plotted with the filled circles, while the IRAS LRS is plotted with the open squares.

**Table 2.** List of calibrators used in the present work, together with 12  $\mu\text{m}$  fluxes ( $F_{12}$ ), uniform-disk diameters ( $d_{\text{UD}}$ ) and the date as well as the time stamp ( $t_{\text{obs}}$ ) of the MIDI observations. The uniform-disk diameters were taken from the CalVin list available at ESO (<http://www.eso.org/observing/etc/>).

Calibrator HD number	$F_{12}$ (Jy)	$d_{\text{UD}}$ (mas)	Date (2004)	$t_{\text{obs}}$ (UTC)
18322	13.3	$2.50 \pm 0.12$	Feb. 09 Feb. 09	00:39:11 01:39:04
49161	10.4	$2.88 \pm 0.17$	Feb. 09 Feb. 10	02:45:52 04:43:21
67582	9.3	$2.69 \pm 0.25$	Feb. 09 Feb. 09 Feb. 10 Feb. 10	06:24:15 07:13:39 02:37:04 03:46:12
107446	32.4	$4.54 \pm 0.23$	Feb. 09 Feb. 10	08:08:53 08:16:44
85951	12.6	$3.48 \pm 0.18$	Feb. 11 Feb. 11	02:42:15 05:37:52
120404	13.3	$3.03 \pm 0.24$	Feb. 11 Feb. 11	07:36:34 08:27:38

using the 47 m baseline between the telescopes UT2 and UT3 (see Tables 1 and 2 for the summary of the observations).

We used two different MIDI data reduction packages: MIA developed at the Max-Planck-Institut für Astronomie and EWS developed at the Leiden Observatory. While the MIA package is based on the power spectrum analysis, which measures the total power of the observed fringes (Leinert et al. 2004), the EWS software first corrects for optical path differences (instrumental as well as atmospheric delays) in each scan, and then, the fringes are coherently added (Jaffe 2004).

Figure 1 shows the calibrated visibilities of IRAS08002 derived from the four data sets. In the figure, the means of the calibrated visibility values derived with the MIA and EWS packages are plotted (the results obtained with two reduction packages are found to be in good agreement for these data sets). The data sets #1 and #3, which were obtained with approximately the same projected baseline lengths and position angles, show good agreement, indicating the good data quality and the reliability of the data reduction procedures. The errors of the calibrated visibilities are typically  $\pm 10$ –15%, and the error sources are described in Ohnaka et al. (2005). Figures 1b–d show the observed visibilities plotted as a function of spatial frequency at three representative wavelengths between 8 and 13  $\mu\text{m}$ , to-

gether with uniform-disk fits. We tentatively fit all the visibility points at a given wavelength with a uniform disk, regardless the position angles, because the limited position angle coverage of the currently available data does not allow us to draw a conclusion about the possible presence or absence of asymmetries. The resulting uniform-disk diameter is plotted as a function of wavelength in Fig. 1e. It should be stressed, however, that we use uniform-disk fits to obtain some kind of representative angular size of the object and that the real intensity distribution of the object can be very different from a uniform disk.

We also extracted the  $N$ -band spectrum of IRAS08002 from the MIDI data, as described in Ohnaka et al. (2005). One of the calibrators, HD 67582 (K3III), for which an absolutely calibrated spectrum is available in Cohen et al. (1999), was observed at similar air masses as IRAS08002 and used as a spectrophotometric standard star. The absolutely calibrated spectrum of IRAS08002 extracted from the MIDI data is shown in Fig. 1f together with the IRAS LRS. The MIDI spectrum shows good agreement with the IRAS LRS, confirming that the silicate emission spectrum has been stable for the last 20 years. This is consistent with the result of the ISO observation by Yamamura et al. (2000), who found that the silicate emission features in another silicate carbon star V778 Cyg were stable for 14 years between the IRAS and ISO observations.

Figure 1 reveals that all visibilities derived from the four data sets show a distinct wavelength dependence: a steady increase from 8 to  $\sim 10 \mu\text{m}$  and a nearly constant part longward of  $10 \mu\text{m}$  with a very slight decrease. This wavelength dependence of the observed visibility translates into roughly constant uniform-disk diameters between 8 and  $10 \mu\text{m}$  and a rather steep increase longward of  $10 \mu\text{m}$ , as shown in Fig. 1e. The wavelength dependence of the visibilities and uniform disk diameters observed in IRAS08002 resembles that observed for the Mira variable RR Sco in the  $N$  band presented in Ohnaka et al. (2005). In the case of RR Sco, Ohnaka et al. (2005) interpret the constant uniform-disk diameters between 8 and  $10 \mu\text{m}$  as due to the optically thick emission from warm, dense layers of  $\text{H}_2\text{O}$  and  $\text{SiO}$  gas extending to  $\sim 2.3 R_\star$ , while the increase of the diameter longward of  $10 \mu\text{m}$  can be attributed to an optically thin dust shell consisting of silicate and corundum. It should be stressed here, however, that this cannot be the case for IRAS08002, because the stellar angular diameter of IRAS08002 is estimated to be  $\sim 1.7 \text{ mas}$  if a linear radius of  $400 R_\odot$  and a distance of 2.2 kpc (Engels 1994) are assumed. It is unlikely that those dense molecular layers extend to the region as far as  $\sim 18\text{--}27 \text{ mas}$  in radius ( $\sim 21\text{--}32 R_\star$ ) from the central star.

The wavelength dependence of the visibility observed for IRAS08002 shows marked contrast to that observed for other objects with a prominent  $10 \mu\text{m}$  silicate feature. Leinert et al. (2004) observed a number of Herbig Ae/Be stars showing the amorphous and crystalline silicate emission features using MIDI. Most of the observed visibilities show a decrease from 8 to  $\sim 9.5 \mu\text{m}$  and a gradual increase longward of  $9.5 \mu\text{m}$ . The visibilities observed for the symbiotic Mira RX Pup also exhibit the same trend (Driebe et al., in preparation). Obviously, the visibilities observed in IRAS08002 show the opposite shape compared to the visibilities observed in these objects.

It should be mentioned here, however, that the current lack of sufficient complementary data on IRAS08002, such as high angular resolution observations by speckle and/or aperture-masking interferometry, high-resolution mid-infrared spectra, and polarimetric observations, makes it difficult to obtain a unique picture of this object. We also note that no radiative transfer model for a circumbinary or circum-companion dust disk around silicate carbon stars has been presented in the literature. Therefore, we start from simple models with silicate dust alone, and after showing that such models have difficulties in reproducing the observations, we propose models with two grain species as possible scenarios.

### 3. Dust radiative transfer code

#### 3.1. Basics of the Monte Carlo code

We have developed a Monte Carlo radiative transfer code (`mcsim_mpi`) and used it for the interpretation of the observations of IRAS08002. Our code `mcsim_mpi` can deal with arbitrary density distributions (spherically symmetric cases, axisymmetric cases, and general three-dimensional cases) as well as multiple grain species which may have different density distributions. Dust with multiple sizes can also be handled with `mcsim_mpi`, which simply treats dust grains of different sizes as different grain species. The calculation of polarization is also included in the code, and its application will be presented in Murakawa et al. (in preparation). The basics of the Monte Carlo technique are well explained somewhere else (e.g., Wolf et al. 1999; Niccolini et al. 2003; Wolf 2003), and therefore, we only briefly describe the outline of the technique.

In the Monte Carlo technique, a number of photon packets are emitted from the surface of the central star with a radius  $R_\star$  and an effective temperature  $T_{\text{eff}}$ , and they travel through the circumstellar dust envelope, interacting with dust grains. We divide the model space into many cells and assume the density and the temperature to be constant in each cell. The initial position of a photon packet on the stellar surface as well as its direction is determined with a random number. The frequency of each initial photon packet is also chosen by a random number so that the spectral shape of emitted photon packets should follow the blackbody radiation of the given effective temperature  $T_{\text{eff}}$ . The energy of each photon packet is given by  $L_\star \Delta t / N$ , where  $L_\star$  is the stellar luminosity,  $\Delta t$  is the time interval of the simulation, and  $N$  is the total number of photon packets. The optical depth ( $\tau_v$ ) which every photon packet can proceed before the next interaction with dust grains (absorption or scattering) is chosen as  $\tau_v = -\ln(1-p)$ , where  $p$  is a random number uniformly distributed between 0 and 1. As the photon packet moves along its path, we calculate the optical depth by

$$\int \sum_{i=1}^{N_{\text{sp}}} \rho_i(\mathbf{r}) (\kappa_{v,i} + \sigma_{v,i}) d\ell,$$

where  $\rho_i(\mathbf{r})$  is the number density of the  $i$ -th grain species at the position  $\mathbf{r}$ ,  $\kappa_{v,i}$  and  $\sigma_{v,i}$  are the absorption and scattering cross sections of the  $i$ -th grain species, respectively, and  $N_{\text{sp}}$  is the number of different grain species. The integration is performed

along the path of the photon packet. The photon packet travels until this accumulated optical depth reaches  $\tau_v$ , the value chosen at the beginning.

When the photon packet reaches the point of the next interaction with dust grains, it undergoes either absorption or scattering. In the presence of multiple grain species, the probability for absorption ( $P_{\text{abs}}$ ) or scattering ( $P_{\text{sca}}$ ) with the  $i$ -th grain species is given by

$$P_{\text{abs}} = \frac{\rho_i(\mathbf{r})\kappa_{v,i}}{\sum_{i=1}^{N_{\text{sp}}} \rho_i(\mathbf{r})(\kappa_{v,i} + \sigma_{v,i})}, P_{\text{sca}} = \frac{\rho_i(\mathbf{r})\sigma_{v,i}}{\sum_{i=1}^{N_{\text{sp}}} \rho_i(\mathbf{r})(\kappa_{v,i} + \sigma_{v,i})},$$

respectively. In the case of scattering, the new direction of the photon packet is determined by a random number so that it samples the phase function of the grain with which the photon packet has just interacted. While our code can deal with arbitrary phase functions, we assume isotropic scattering throughout the present work for simplicity. In the case of absorption, we adopt the temperature correction scheme developed by Bjorkman & Wood (2001). In their method, the energy of the photon packet just absorbed by a dust grain is used to calculate the dust temperature, and the photon packet is re-emitted immediately. The new direction is isotropically chosen, and the new frequency is chosen so that the re-emitted photon packet corrects the temperature of the spectrum previously emitted by the cell. This scheme accelerates a Monte Carlo simulation dramatically (provided that the opacity is independent of temperature). When the photon packet finally escapes the circumstellar envelope toward a given viewing angle, its final frequency is registered within  $N_v$  frequency bins which are distributed equidistantly in the logarithmic scale between  $\nu_{\text{min}}$  and  $\nu_{\text{max}}$ . In the calculations presented here, we set  $N_v$ ,  $\nu_{\text{min}}$ , and  $\nu_{\text{max}}$  to be 256,  $3 \times 10^{11}$  Hz (1000  $\mu\text{m}$ ), and  $3 \times 10^{15}$  Hz (0.1  $\mu\text{m}$ ), respectively.

Our code `mcsim_mpi` is parallelized with the use of LAM/MPI<sup>3</sup>, which coordinates the code to run on different machines connected by the network. Specifically, a Monte Carlo simulation is started on each machine with a different random seed. After the simulations on all the machines are completed, the results obtained on all the machines are collected, and the averages of the results such as temperature distributions, SEDs and images are calculated.

After all photons have escaped the envelope, we store the monochromatic mean intensity ( $J_\nu$ ) and the temperature in each cell so that images at a given wavelength viewed from an arbitrary angle can be created by ray tracing. Lucy (1999) shows that the mean intensity in a particular cell is given by

$$J_\nu d\nu = \frac{1}{4\pi} \frac{1}{V} \frac{L_\star}{N} \sum_{d\nu} \ell,$$

where  $V$  is the volume of the cell, and the summation is over all path lengths within the cell at issue for all photon packets with frequencies in  $(\nu, \nu + d\nu)$ . With the monochromatic mean intensity and the temperature in each cell available, it is straightforward

to calculate the intensity expected for any line of sight by ray tracing, which is expressed as

$$I_\nu = I_\nu^\star + \int S_\nu e^{-\tau_\nu} d\tau_\nu, \quad I_\nu^\star = B_\nu(T_{\text{eff}}) e^{-\tau_\nu^\star},$$

where  $\tau_\nu^\star$  is the optical depth from the observer to the stellar surface along the line of sight defined by the viewing angle of the observer, and the integration is performed along this line of sight. The  $I_\nu^\star$  term, which represents the intensity coming from the central star, must be added if the line of sight intersects with the central star. Otherwise this term is set to zero.  $S_\nu$  is the source function and, in the case of isotropic scattering, given by

$$S_\nu = \frac{\sum_{i=1}^{N_{\text{sp}}} \rho_i(\mathbf{r})(\kappa_{v,i} B_\nu(T_i(\mathbf{r})) + \sigma_{v,i} J_\nu(\mathbf{r}))}{\sum_{i=1}^{N_{\text{sp}}} \rho_i(\mathbf{r})(\kappa_{v,i} + \sigma_{v,i})},$$

where  $T_i(\mathbf{r})$  is the temperature of the  $i$ -th grain species at the position  $\mathbf{r}$ , and  $B_\nu(T_i(\mathbf{r}))$  is the Planck function of that temperature.

Images thus produced using the ray-tracing technique are of much better S/N ratios compared to those created directly by collecting photons escaping the envelope during a Monte Carlo simulation. In the model calculations for IRAS08002, we use  $\sim 10^6 - 5 \times 10^7$  photon packets, which produce SEDs as well as ray-tracing images with sufficient S/N ratios.

### 3.2. Tests in spherically symmetric cases

In order to check the reliability of the `mcsim_mpi` code, we performed test calculations in spherically symmetric cases and compared the results with those obtained with the DUSTY code, which is a publicly available radiative transfer program for spherically symmetric cases (Ivezić & Elitzur 1997). The spectrum of the central star is represented by blackbody radiation, and an effective temperature of 3000 K is assumed. The luminosity of the central star is set to  $10^4 L_\odot$ . The absorption and scattering cross sections are calculated from the complex refractive index of the warm silicate dust (Ossenkopf et al. 1992) in the Mie theory for a single grain size of 0.1  $\mu\text{m}$ , using the code of Bohren & Huffman (1983). Throughout the present work, we use 0.55  $\mu\text{m}$  as a reference wavelength for the optical depth, and the optical depths ( $\tau_\nu$ ) used for the test calculations are 1, 10, and 100. The dust density is assumed to be proportional to  $r^{-2}$ . The inner boundary of the dust shell ( $r_{\text{in}}$ ) is defined as a radius where the dust temperature is equal to a pre-given dust sublimation temperature, for which we adopt 1000 K. The outer boundary ( $r_{\text{out}}$ ) is set to be  $10^3 \times r_{\text{in}}$ .

For the calculations with `mcsim_mpi`, five 1.8 GHz Linux PCs are used, with  $2 \times 10^6$  photon packets emitted on each machine. The dust envelope is divided into 100 cells in the radial direction, equidistantly on the logarithmic scale. We use the inner boundary radius derived with the DUSTY code as the input of our `mcsim_mpi` code. Figure 2 shows the SEDs and temperature distributions calculated with `mcsim_mpi` and DUSTY. Note that these SEDs are scaled to the values expected at the distance equal to the stellar radius defined as  $(L_\star/4\pi\sigma T_{\text{eff}}^4)^{1/2}$ ,

<sup>3</sup> <http://www.lam-mpi.org>

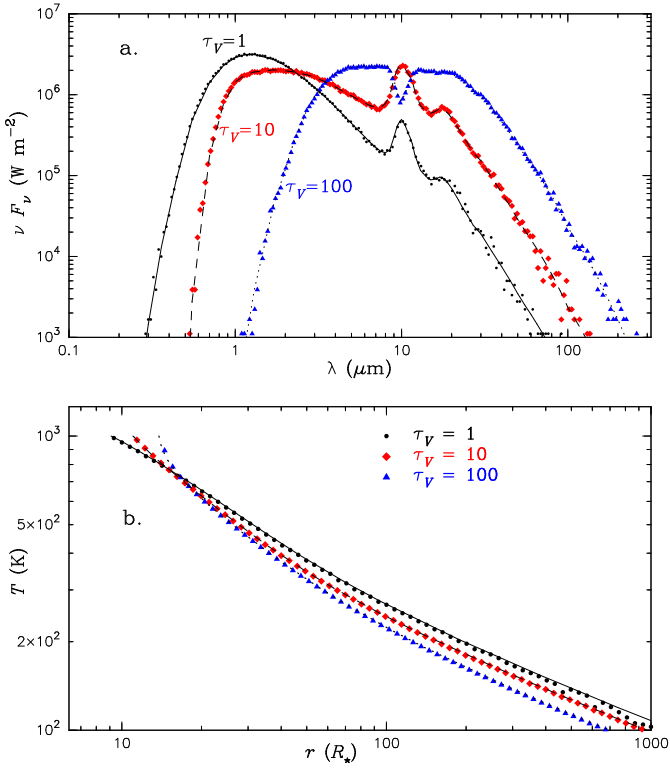


**Fig. 2. a:** Comparison between the SEDs calculated with `mcsim_mpi` (see Sect. 3.1) and DUSTY for three different optical depths. The effective temperature of the central star and the inner boundary temperature of the dust shell are set to be 3000 K and 1000 K, respectively. The results obtained with DUSTY are represented with the solid, dashed, and dotted lines, while the results obtained with `mcsim_mpi` are represented with the dots, filled diamonds, and filled triangles. **b.** Comparison between the temperature distributions calculated with `mcsim_mpi` and DUSTY. The meanings of the symbols are the same as in the panel **a**.

where  $\sigma$  is the Stefan-Boltzmann constant. The figure illustrates that the results obtained with both codes show good agreement in the three cases, demonstrating the reliability of the `mcsim_mpi` code.

### 3.3. Test in axisymmetric cases

We further test our `mcsim_mpi` code in axisymmetric cases. Pascucci et al. (2004) performed benchmark test calculations using five different multi-dimensional radiative transfer codes for a flattened, torus-like density distribution. We compare the result obtained with our `mcsim_mpi` code with the results of these benchmark tests using the same density distribution and input parameters. We calculate the model with  $\tau_V = 100$  in the equatorial direction, the highest optical depth in the models presented by Pascucci et al. (2004). Figure 3a shows a comparison of SEDs viewed from two different inclination angles (the inclination angle  $i$  is measured from the symmetry axis of the dust density distribution throughout the present work):  $i = 12.5^\circ$  (viewed nearly pole-on) and  $i = 77.5^\circ$  (viewed nearly edge-on). These SEDs are scaled to the values expected at the distance of the stellar radius. Figure 3b shows the tempera-

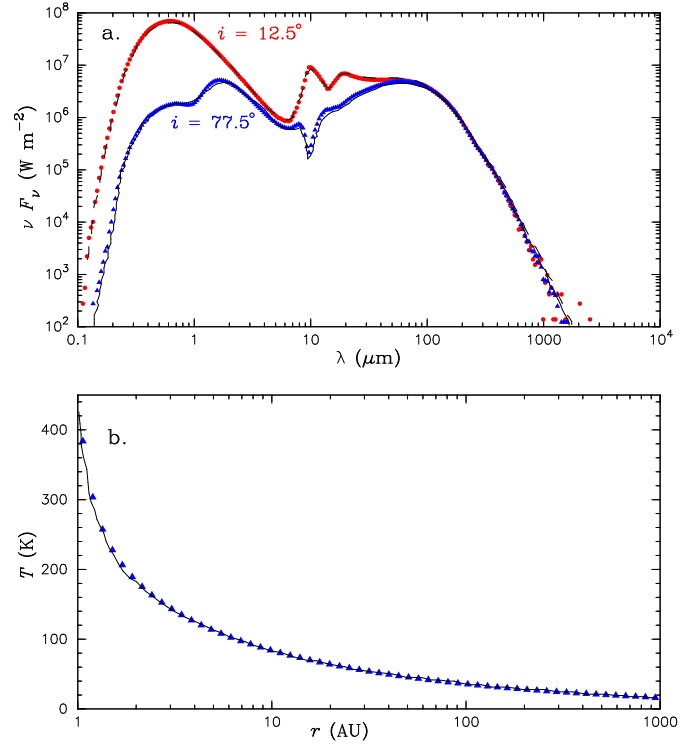


**Fig. 3.** Comparison between the results obtained with `mcsim_mpi` and the results of the benchmark tests for  $\tau_V = 100$  published in Pascucci et al. (2004). **a.** Comparison of the SEDs calculated for two different inclination angles. The results of the benchmark tests of Pascucci et al. (2004) are plotted with the solid and dashed lines, while the results obtained with `mcsim_mpi` are plotted with the filled circles and filled triangles. **b.** Comparison of the temperature distributions obtained with `mcsim_mpi` and the benchmark tests. The solid line represents the radial temperature distribution of the benchmark tests predicted for an angle of  $2.5^\circ$  measured from the equatorial plane. The corresponding temperature distribution obtained with `mcsim_mpi` is represented with the filled triangles.

ture distribution in the nearly equatorial direction. These figures demonstrate that the agreement between the results obtained with `mcsim_mpi` and the results of the benchmark tests of Pascucci et al. (2004) is good.

## 4. Models with silicate dust alone

Using the Monte Carlo radiative transfer code described above, we calculate SEDs as well as  $N$ -band visibilities and compare with the observations of IRAS08002. The effective temperatures of IRAS08002 derived by previous authors are 2500 K (Kwok & Chan 1993) and 3015 K (Bergeat et al. 2002). In the present work, we assume the effective temperature to be 2750 K, the mean value of this range. The luminosity of the central star is set to be  $10^4 L_\odot$ , assuming that the central star (the primary star with a carbon-rich photosphere) is the only heating source. It would be reasonable to neglect the contribution of the putative companion, because its luminosity is considered to be much lower than that of the primary star. For the dust opacity, we use the warm silicate dust of Ossenkopf et al. (1992) with a single grain size of  $0.1 \mu\text{m}$ .



First, we attempt to explain the observed SED and  $N$ -band visibilities using axisymmetric disk models (including spherical shell models as special cases) consisting of silicate dust alone. As depicted in the inset of Fig. 4a, we represent this dust disk with a sphere from which a bipolar cavity is carved out. Within the disk, the density depends only on the distance from the central star, while it is set to zero in the bipolar cavity. We split the disk into 100–200 cells in the radial direction and 18–36 cells in the latitudinal direction within the disk. The free parameters are the inner boundary radius ( $r_{\text{in}}$ ), the optical depth in the equatorial direction ( $\tau_{\text{V}}^{\text{sil}}$ ), the disk half-opening angle measured from the equatorial plane ( $\Theta$ ), and the exponent of the radial density distribution (density proportional to  $r^{-p}$ ). The ranges of the changes of these parameters are  $r_{\text{in}} = 10 \dots 25 R_{\star}$  with  $\Delta r_{\text{in}} = 5 R_{\star}$ ,  $\tau_{\text{V}}^{\text{sil}} = 5 \dots 25$  with  $\Delta \tau_{\text{V}}^{\text{sil}} = 5$ ,  $\Theta = 10^{\circ} \dots 90^{\circ}$  with  $\Delta \Theta = 20^{\circ}$ , and  $p = 1.2 \dots 2$  with  $\Delta p = 0.2$ . Note that a model with a disk half-opening angle ( $\Theta$ ) of  $90^{\circ}$  corresponds to a spherical shell model. The outer boundary radius is set to  $500 \times r_{\text{in}}$ . This parameter has only minor effects on the SEDs in the wavelength range considered in the present work and  $N$ -band visibilities and, therefore, cannot be well constrained. The SEDs for 5–10 different inclination angles ( $i$ , as defined in Sect. 3.3) between  $0^{\circ}$  and  $90^{\circ}$  are calculated. For each model, we first compare the SEDs calculated for different inclination angles with the observed SED. For models which can reproduce the observed SED reasonably well, we produce images and visibilities in the  $N$  band.

Figure 4a shows an example of the models which can reproduce the observed SED rather well. The parameters of this model are  $\tau_{\text{V}}^{\text{sil}} = 15$ ,  $r_{\text{in}} = 15 R_{\star}$ ,  $p = 1.4$ , and  $\Theta = 50^{\circ}$ , and the SED plotted in Fig. 4a was calculated for an inclination angle of  $30^{\circ}$ . The observed SED is constructed from the photometric data of Le Bertre et al. (1990) as well as the IRAS fluxes, together with the IRAS LRS. As for the interstellar extinction toward IRAS08002, Kwok & Chan (1993) derived  $A_{\text{V}} = 1.5$  from the SED fitting, while Bergeat et al. (2002) derived  $A_{\text{J}} = 0.32$ , which translates into  $A_{\text{V}} = 1.1$  with  $A_{\text{J}} = 0.87E(B - V)$  and  $A_{\text{V}} = 3.1E(B - V)$  (Savage & Mathis 1979). These values are in agreement with the results obtained by Neckel & Klare (1980) for the estimated distance of IRAS08002 of 2.2 kpc. The photometric data of Le Bertre et al. (1990) are de-reddened using the method of Savage & Mathis (1979) with  $A_{\text{V}} = 1.5$  (open squares in Fig. 4). We also plot the original data of Le Bertre et al. (1990) to show the effect of the interstellar extinction (filled squares). Note that the correction for the interstellar extinction is negligible at wavelengths longer than the  $L$  band. The model flux is higher than the observed data at wavelengths shorter than  $\sim 1 \mu\text{m}$ , but this may be attributed to the uncertainty of the effective temperature of the central star as well as the use of the blackbody for the stellar spectrum, neglecting the molecular absorption seen in usual carbon stars.

It should be noted here that spherical shell models, which are special cases with  $\Theta = 90^{\circ}$ , cannot reproduce the observed SED and  $N$ -band visibilities. We found that the models, which can reproduce the SED from the near- to the far-infrared, predict the flux at wavelengths shorter than  $\sim 1 \mu\text{m}$  to be considerably lower than the observations, that is, the central star appears to be too obscured. This means that in the spherically symmet-

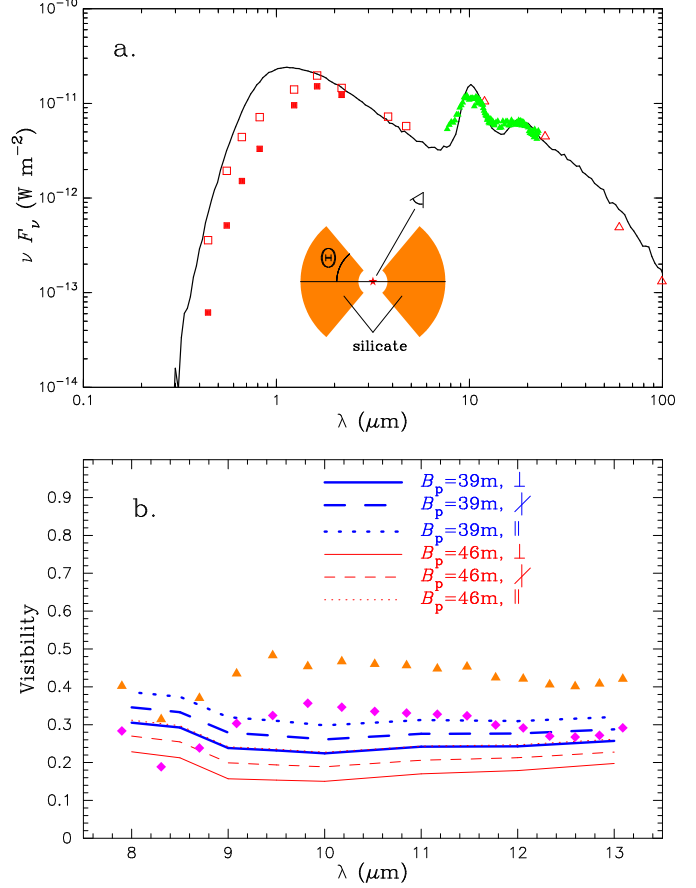


**Fig. 4.** Axisymmetric disk model consisting of silicate dust alone. The parameters of the model are  $\tau_{\text{V}}^{\text{sil}} = 15$ ,  $r_{\text{in}} = 15 R_{\star}$  (30 AU),  $\Theta = 50^{\circ}$ , and a radial density distribution proportional to  $r^{-1.4}$ . The model SED and visibilities are calculated for an inclination angle of  $30^{\circ}$  (measured from pole-on). **a.** The observed SED is shown by the open squares (Le Bertre et al. 1990, de-reddened with  $A_{\text{V}} = 1.5$ ), open triangles (IRAS), and filled triangles (IRAS LRS). The original data of Le Bertre et al. (1990), not corrected for the interstellar extinction, are also plotted with the filled squares. The model SED is represented with the solid line. **b.** Filled triangles and diamonds:  $N$ -band visibilities measured with the 39 m and 46 m baselines (data sets #2 and #3), respectively. Thick and thin lines (solid, dashed, and dotted) represent the visibilities predicted for projected baseline lengths of 39 and 46 m, respectively. The solid, dashed, and dotted lines represent the model visibilities predicted for different position angles (solid line: perpendicular to the symmetry axis of the model intensity distribution, dotted line: parallel to the symmetry axis, dashed line:  $45^{\circ}$  with respect to the symmetry axis). See also Sect. 4 and Fig. 6.

ric geometry, the amount of silicate dust necessary to account for the observed infrared excess is not consistent with the low extinction toward the central star. As Lloyd-Evans (1990) argues, this indicates that dust may exist in a disk, instead of a spherical shell. Although the agreement at optical wavelengths can be somewhat improved by adopting an effective temperature of 3000 K, it has turned out that such spherical models cannot reproduce the MIDI observations like the disk models discussed below.

The visibilities expected from the model shown in Fig. 4a are shown in Fig. 4b as a function of wavelength. We need to

estimate the angular radius of the central star to compare the predicted visibilities with the MIDI observations. We note that the model SEDs are scaled to fit the observed fluxes, and this scaling factor is given by  $(R_*/d)^2$ , where  $d$  is the distance to IRAS08002, and  $R_*/d$  is the angular radius of the central star. Using this angular radius, we can obtain model visibilities by calculating the two-dimensional Fourier transform of the intensity distribution of the object at a given wavelength, which is produced with the ray-tracing method described in Sect. 3. We also note here that since the model intensity distributions are not centrosymmetric except for models with  $\Theta = 90^\circ$ , we need to specify the position angle of the symmetry axis of the disk relative to north to compare with the MIDI observations. This is equivalent to specifying the angle between the symmetry axis of the disk (projected onto the plane of the sky) and the projected baseline vector used in observations, and we use this angle as a free parameter. The dotted lines in Fig. 4b represent the visibilities calculated with projected baseline vectors parallel to the symmetry axis of the disk in the plane of the sky, while the solid lines represent those calculated with projected baseline vectors perpendicular to the symmetry axis. The dashed lines represent the visibilities calculated with projected baseline vectors at  $45^\circ$  with respect to the symmetry axis (see also Fig. 6 for the illustration of the orientation of these baseline vectors). In other words, for the cases plotted with the dotted, dashed, and solid lines, the position angles of the disk axis relative to north are given by P.A., P.A. $\pm 45^\circ$ , and P.A. $\pm 90^\circ$ , respectively, where P.A. is the position angle of a projected baseline used in our MIDI observations. The dotted and solid lines represent the full range of visibilities predicted for different position angles of the disk, and we check whether the observed visibilities can be reproduced within this range.

Figure 4b reveals that this disk model fails to reproduce the MIDI observations. The model predicts the visibilities to decrease from 8 to 10  $\mu\text{m}$ , in clear disagreement with the MIDI observations. The optical depths of the disk models are larger at 10  $\mu\text{m}$  than at 8  $\mu\text{m}$ , due to the prominent silicate feature. Also, the flux contribution of the central star is larger at 8  $\mu\text{m}$  than at 10  $\mu\text{m}$ . Therefore, if the spatial distribution of silicate dust is extended, as in the case of the models here, the angular size at 10  $\mu\text{m}$  becomes remarkably larger than at 8  $\mu\text{m}$ . A significant increase of the optical depth makes the decrease of the visibility from 8 to 10  $\mu\text{m}$  less steep, but it cannot reproduce the observed increase, and the silicate emission spectrum also appears distorted. With a simple disk geometry used in the present work, we could not find a parameter set which can simultaneously reproduce the observed SED and the  $N$ -band visibilities. We also calculated disk models whose density distributions are proportional to  $r^{-p} \times \exp(-(\theta/\Theta_0)^2)$ , where  $\Theta_0$  is a constant to define the geometrical thickness of the disk, and  $\theta$  is the latitudinal angle measured from the equatorial plane. However, the model visibilities show the same trend as found in the above models. As for the possible effects of more complicated disk geometries, we note here that Leinert et al. (2004) present the  $N$ -band visibilities of Herbig Ae/Be stars (showing the 10  $\mu\text{m}$  silicate feature) predicted by disk models with more realistic geometries such as the puffed-up rims and self-shadowing taken into account. Still, these model visibilities are characterized by a

steep decrease from 8 to 10  $\mu\text{m}$  and a plateau with a slight increase up to 13  $\mu\text{m}$ , which is obviously in disagreement with the MIDI observations of IRAS08002. Of course, the temperatures of the central stars of these Herbig Ae/Be stars as well as the physical properties of the disks are very different from those of IRAS08002. Therefore, while we cannot completely exclude the possibility that more complicated disk geometries may partially explain the MIDI observations of IRAS08002, and this possibility should be examined when more observational constraints become available, it seems unlikely that disk (and also spherical shell) models consisting of silicate dust alone can fully explain the observed SED and  $N$ -band visibilities.

## 5. Models with two grain species

As a possible scenario to explain the observed SED and  $N$ -band visibilities, we consider models with two grain species, silicate and some other grain species. Since the IRAS LRS and MIDI spectrum do not show prominent features other than the broad 10  $\mu\text{m}$  feature, we tentatively consider the following three grain species, which exhibit no conspicuous spectral features in the wavelength range covered by these spectra.

The first candidate is amorphous carbon. Given the fact that the central star is a carbon star, it is well possible that the circumstellar environment may have mixed chemistry consisting of oxygen-rich dust (silicate) and carbon-rich dust resulting from the current mass loss. The second candidate is large silicate grains. The opacity of a spherical grain with a radius  $a$  becomes flat at wavelengths shorter than  $\sim 2\pi a$ , showing little wavelength dependence. This means that large silicate grains ( $a \gtrsim 3 \mu\text{m}$ ) do not show the 10  $\mu\text{m}$  and 18  $\mu\text{m}$  features and can be a candidate for the second grain species. There is also observational evidence for the presence of large grains in the circumstellar environment of silicate carbon stars, as discussed in Sect. 5.2. The third candidate is metallic iron. The theoretical calculations of dust formation by Gail & Sedlmayr (1999) suggest that metallic iron, which has a condensation temperature only by 50–100 K lower than that of silicate, can form in oxygen-rich AGB winds as separate grains or as inclusions within silicate grains. There is also observational evidence suggestive of the presence of metallic iron in the circumstellar envelope of cool, evolved stars (e.g., Harwit et al. 2001; Kemper et al. 2002; see also Sect. 5.3).

We note here that crystalline silicate was identified in the silicate carbon star IRAS09425-6040 (Molster et al. 1999, 2001). The slight hump at  $\sim 11.5 \mu\text{m}$  seen in the spectra of IRAS08002 coincides with the position of a crystalline silicate feature. However, since IRAS08002 was not observed with ISO, and the IRAS LRS as well as the MIDI spectrum is of low spectral resolution, it is not possible to confirm the presence of crystalline silicate unambiguously. Thus, while we stress the importance of high-resolution mid-infrared spectroscopy to confirm the presence or absence of crystalline silicate toward IRAS08002, we do not consider models with crystalline silicate in the present work.



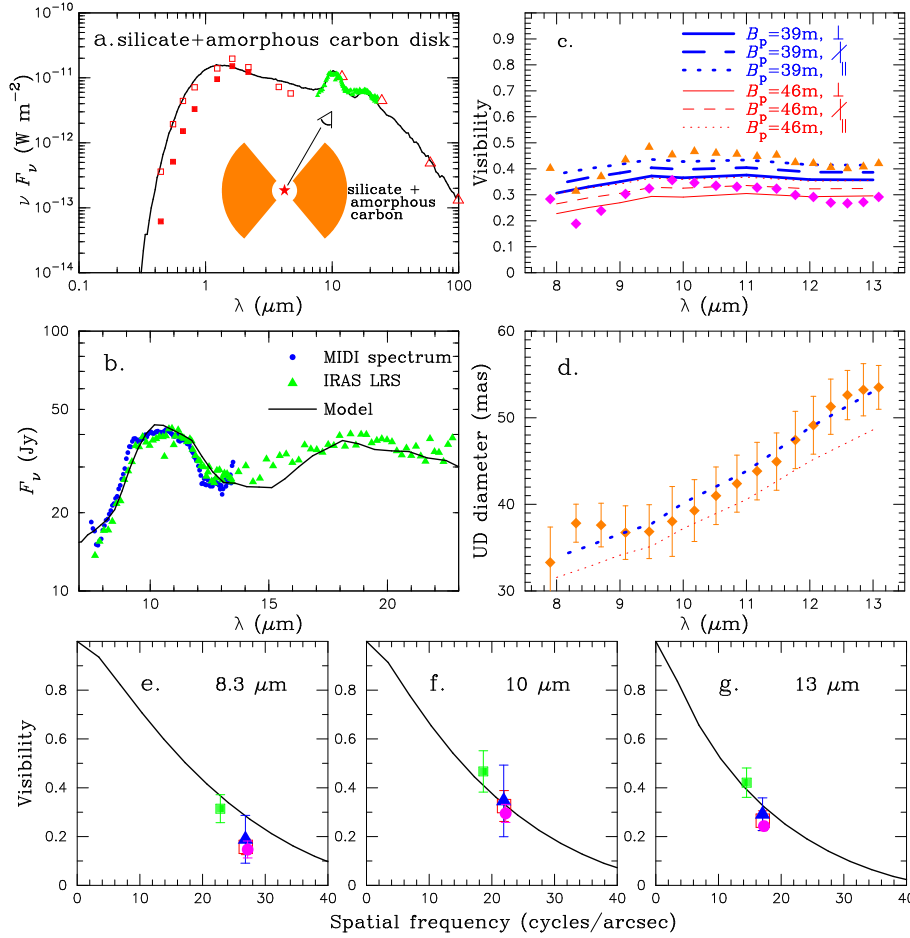


**Fig. 5.** The best-fit disk model consisting of silicate and amorphous carbon (see Sect. 5.1). The parameters of the model are  $\tau_V^{\text{sil}} = 25$ ,  $\tau_V^{\text{amc}} = 15$ ,  $r_{\text{in}} = 15 R_\star$  (30 AU),  $p = 1.6$ , and  $\Theta = 50^\circ$ . The model SED and visibilities are calculated for an inclination angle of  $30^\circ$ . See also the legend to Fig. 4 for the references of the symbols. **a.** Comparison between the observed and model SEDs. **b.** Comparison between the observed silicate emission spectra and the predicted spectrum. **c.** Filled triangles and diamonds:  $N$ -band visibilities measured with the 39 m and 46 m baselines, respectively. Thick and thin lines (solid, dashed, and dotted) represent the corresponding model visibilities. See the legend to Fig. 4 for the meanings of the different line types. **d.** The observed uniform-disk diameters are plotted with the filled diamonds. The thick and thin dotted lines represent the uniform-disk diameters predicted for the 39 m and 46 m baselines, respectively, with the baseline vector parallel to the symmetry axis. **e.–g.** The model visibilities predicted with the baseline vector parallel to the symmetry axis are plotted (solid lines) together with the observed visibilities. See Fig. 1 for the references of the symbols.

### 5.1. Models with silicate and amorphous carbon

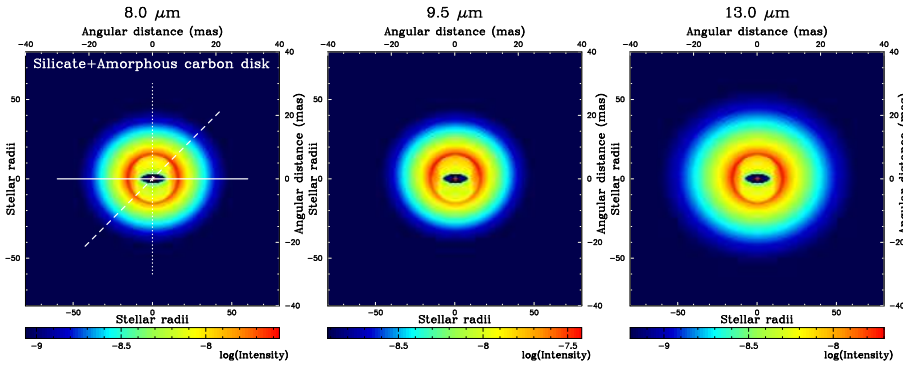
Firstly, we examine models containing silicate and amorphous carbon. At the moment, we assume that the two grain species coexist in an axisymmetric disk, as depicted in the inset of Fig. 5a (another possible geometry is discussed later). The free parameters in this geometry are the same as described in Sect. 4, except that we now have an additional parameter to specify the optical depth of amorphous carbon in the radial direction ( $\tau_V^{\text{amc}}$ ). The density distributions of silicate and amorphous carbon grains are assumed to be proportional to  $r^{-p}$ . The warm silicate dust of Ossenkopf et al. (1992) and the amorphous carbon of Rouleau & Martin (1991) are used, with a grain size of  $0.1 \mu\text{m}$  adopted for both grain species. The ranges of the changes of the parameters are as follows:  $\tau_V^{\text{sil}} = 15 \dots 35$  with  $\Delta\tau_V^{\text{sil}} = 5$ ,  $\tau_V^{\text{amc}} = 5 \dots 25$  with  $\Delta\tau_V^{\text{amc}} = 5$ ,  $r_{\text{in}} = 10 \dots 25 R_\star$  with  $\Delta r_{\text{in}} = 5 R_\star$ ,  $\Theta = 10^\circ \dots 90^\circ$  with  $\Delta\Theta = 20^\circ$ , and  $p = 1.4, 1.6, 1.8, 2.0$ . The outer boundary radius is fixed to  $500 \times r_{\text{in}}$ , because the effects of this parameter on SEDs and  $N$ -band visibilities are minor, and therefore, it cannot be well constrained by the observational data available at the present.

Figure 5 shows the results obtained by the best-fit model in this geometry. The disk inner radius is found to be  $15 R_\star$ , while the exponent of the density distribution of silicate and amorphous carbon dust is derived to be 1.6. The optical depths of silicate and amorphous carbon dust are found to be 25 and 15 at  $0.55 \mu\text{m}$  (1.9 and 0.1 at  $10 \mu\text{m}$ ), respectively. The disk half-

opening angle and the inclination angle are found to be  $50^\circ$  and  $30^\circ$ , respectively. We estimate the uncertainties of these parameters by varying them by a small amount around the parameter set of the best-fit model. The uncertainties of the optical depths and the inner boundary radius are estimated to be approximately 20%. The uncertainty of  $p$  is estimated to be roughly  $\pm 0.1$ . We estimate the uncertainty of the disk half-opening angle and that of the inclination angle to be roughly  $\pm 10^\circ$ .

Figures 5a and 5b show that the model SED is in fair agreement with the observed one in the wavelength range from the optical to the far-infrared. Figures 5c and 5e–g show a comparison between the observed  $N$ -band visibilities and those predicted by this model. Given the errors of the observed visibilities (see Figs. 5e–g), the visibilities predicted for the baseline vector with  $45^\circ$  or parallel with respect to the symmetry axis (dashed and dotted lines in Fig. 5c, respectively) can approximately reproduce the observed  $N$ -band visibilities, although the predicted visibilities tend to be flatter than the observations between 8 and  $10 \mu\text{m}$  (this point will be discussed in Sect. 6). This rough agreement can also be seen in Fig. 5d, where a comparison between the observed and predicted uniform-disk diameters is shown.

The reason this model with two grain species can fairly reproduce the observed wavelength dependence of the  $N$ -band visibilities can be explained as follows. We first note that the model intensity distribution of the amorphous carbon component is more extended than that of the silicate component, be-



**Fig. 6.** The mid-infrared images predicted by the best-fit model containing silicate and amorphous carbon dust. In each image, the color scale is normalized with the maximum intensity (excluding the central star) and the minimum intensity set to  $3 \times 10^{-2} \times$  maximum intensity (the color scale on the central star is saturated). The model parameters are given in the legend to Fig. 5 as well as in Sect. 5.1. The solid, dashed, and dotted lines in the left panel illustrate the orientation of the baseline vectors used in the visibility calculations.

cause the high optical depth of this latter component makes the temperature gradient in the radial direction steeper than that of the former component. The total visibility is the weighted sum of the visibilities of these two components. The weights of both components are given by the ratio of the fractional fluxes of the two components, which varies significantly between 8 and 13  $\mu\text{m}$  due to the 10  $\mu\text{m}$  silicate feature. Combination of this variation of the flux contributions of both components and their different angular sizes (and also different wavelength dependences of the angular sizes) results in the  $N$ -band visibilities which are very different from those expected from disk models with silicate dust alone, and that can approximately reproduce the MIDI observations. Figure 6 shows the images at 8, 9.5, and 13  $\mu\text{m}$  predicted by the best-fit model with silicate and amorphous carbon. The images at 8 and 9.5  $\mu\text{m}$  are of approximately the same size, while the image at 13  $\mu\text{m}$  appears more extended than those at 8 and 9.5  $\mu\text{m}$ , corresponding to the wavelength dependence of the observed uniform-disk diameters.

The temperatures of silicate and amorphous carbon dust at the inner boundary of the disk are approximately 730 and 900 K, respectively. The temperature of silicate dust is remarkably lower than condensation temperatures of silicate of  $\sim 1000$  K derived for AGB stars with high mass-loss rates ( $\dot{M} \gtrsim 5 \times 10^{-5} M_{\odot} \text{ yr}^{-1}$ ), but in agreement with the inner boundary temperatures found for objects with lower mass-loss rates (e.g., Lorenz-Martins & Pompeia 2000; Suh 2004). The temperature of amorphous carbon found here is also lower than most of the values ( $\sim 1500$  K) derived for carbon stars by Groenewegen (1995) and Groenewegen et al. (1998), but not exceptionally low. It should be noted, however, that the temperature at the disk inner boundary may not necessarily correspond to the condensation temperatures of these grain species, because dust formation in such a disk as considered here can be different from that expected in mass outflows in usual AGB stars.

The total dust mass in the above model is  $3.0 \times 10^{-3} M_{\odot}$  (silicate) and  $6.6 \times 10^{-4} M_{\odot}$  (amorphous carbon), with bulk densities of  $3.7 \text{ g cm}^{-3}$  and  $2.3 \text{ g cm}^{-3}$  assumed for silicate and amorphous carbon, respectively. This translates into a total disk mass of  $0.4 M_{\odot}$  with a gas-to-dust-ratio of 100. However, the estimated disk mass depends on the assumed outer boundary radius. With an outer boundary radius of  $10^3 \times r_{\text{in}}$ , which can also provide reasonable agreement with the observations, the disk mass increases to  $0.9 M_{\odot}$ . If we assume a mass loss rate

of the order of  $10^{-6} - 10^{-5} M_{\odot} \text{ yr}^{-1}$  (dust mass loss rate  $\sim 10^{-8} - 10^{-7} M_{\odot} \text{ yr}^{-1}$ ) for the primary star in its oxygen-rich phase, the above mass of silicate dust can be accumulated in  $\sim 10^5$  yr, if all material shed by mass loss is stored in the disk. While the lifetime of the circumbinary disk is uncertain, this time scale of mass loss seems to be plausible in terms of the time scale of stellar evolution at the AGB.

One concern with this model is the rather high optical depth of amorphous carbon dust ( $\tau_{\text{V}}^{\text{amc}} \simeq 15$ ) and its connection to the current mass loss rate of the central star, which is now a carbon-rich AGB star. While such a high optical depth is not uncommon among dust-enshrouded carbon stars (e.g., Groenewegen et al. 1998; Lorenz-Martins et al. 2001), the mass loss rates found in those objects are also rather high in general ( $\dot{M} \gtrsim 10^{-5} M_{\odot} \text{ yr}^{-1}$ ), and the central stars are heavily obscured by thick dust shells. However, the observed SED of IRAS08002 does not suggest that the central star is significantly obscured. Therefore, if the current mass loss rate of IRAS08002 is of the order of  $10^{-5} M_{\odot} \text{ yr}^{-1}$ , the mass loss may not be spherically symmetric. This means that the current (carbon-rich) mass loss may be taking place preferably toward the disk, which was presumably formed by oxygen-rich material previously shed by the primary star. However, the mass loss phenomenon in binary systems, in particular with a (circumbinary) disk, is not well understood, and it still remains to be studied whether the mass outflow can be directed toward the disk.

We also calculated models where silicate grains are present in such a disk as considered above but amorphous carbon is distributed in a spherical shell resulting from the current mass loss of the central carbon star. In these models, the inner boundary radii for both grain species are set to be equal for simplicity. However, we could not find a parameter set that can provide reasonable agreement with the observed SED and  $N$ -band visibilities. This is because the high optical depths of the amorphous carbon shell lead to significant obscuration of the central star, which is in disagreement with the observed SED of IRAS08002 as discussed above. If we decrease the optical depth of the amorphous carbon shell to match the observed SED, the model then approaches the disk model consisting only of silicate dust described in Sect. 4 and fails to reproduce the MIDI observations. However, since we cannot entirely exclude the possibility that more complicated disk geometries together with the amorphous carbon shell as well as addition of another

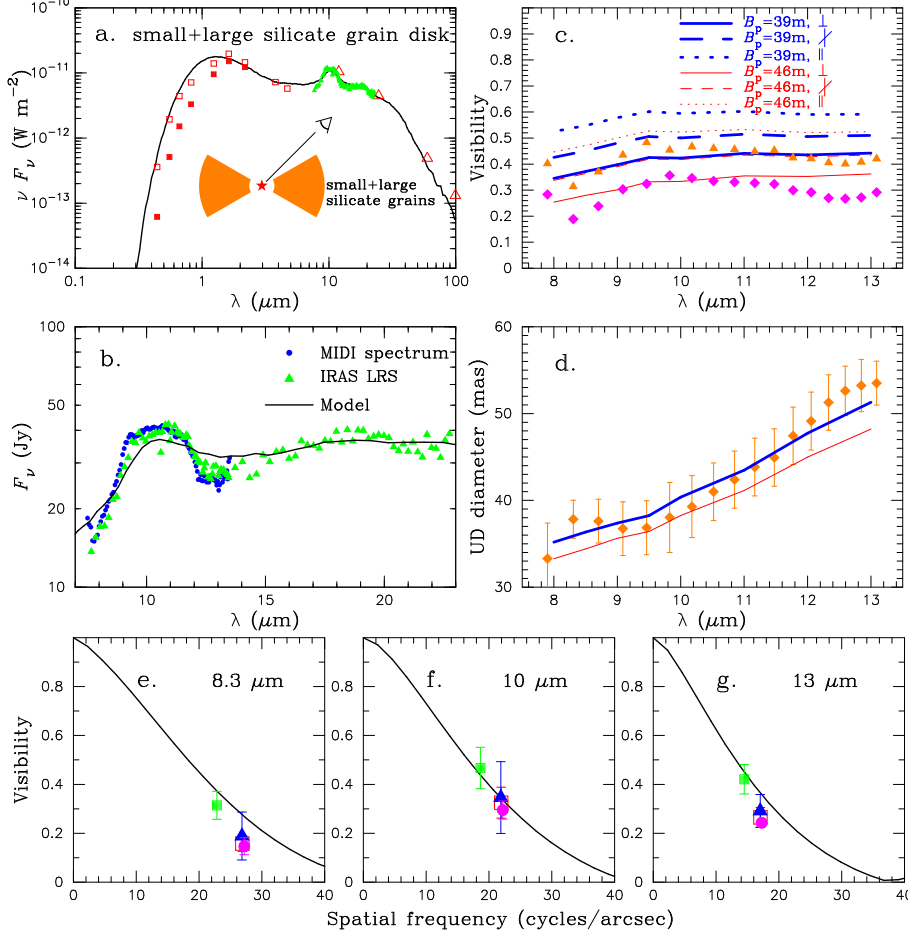


**Fig. 7.** The best-fit disk model consisting of small and large silicate grains (see Sect. 5.2). The parameters of the model are  $\tau_V^{\text{sil}} = 25$ ,  $\tau_V^{\text{SIL}} = 2.0$ ,  $r_{\text{in}} = 15 R_\star$  (30 AU),  $p = 1.8$ , and  $\Theta = 30^\circ$ . The model SED and visibilities are calculated for an inclination angle of  $45^\circ$ . See also the legend to Fig. 4 for the references of the symbols. **a.** Comparison between the observed and model SEDs. **b.** Comparison between the observed silicate emission spectra and the predicted spectrum. **c.** Filled triangles and diamonds:  $N$ -band visibilities measured with the 39 m and 46 m baselines, respectively. Thick and thin lines (solid, dashed, and dotted) represent the corresponding visibilities. See the legend to Fig. 4 for the meanings of the different line types. **d.** The observed uniform-disk diameters are plotted with the filled diamonds. The thick and thin solid lines represent the uniform-disk diameters predicted for the 39 m and 46 m baselines, respectively, with the baseline vector perpendicular to the symmetry axis. **e.–g.** The model visibilities predicted with the baseline vector perpendicular to the symmetry axis are plotted (solid lines) together with the observed visibilities. See Fig. 1 for the references of the symbols.

grain species might explain the observations, more observational data are needed to test such complicated models.

## 5.2. Models with small and large silicate grains

Secondly, we present models consisting of small and large silicate grains. The spatial distributions of the two grain species are the same as used in the previous subsection, except that large silicate grains, instead of amorphous carbon, coexist with small silicate grains in the disk. The spatial distributions of small and large silicate grains may not entirely overlap due to dust formation and growth processes, but we adopt this geometry for simplicity in the present work. We use the opacity of the warm silicate (Ossenkopf et al. 1992) and tentatively adopt a grain size of  $5 \mu\text{m}$  for large silicate grains and  $0.1 \mu\text{m}$  for small silicate grains. The optical depths of small and large silicate grains are denoted as  $\tau_V^{\text{sil}}$  and  $\tau_V^{\text{SIL}}$ , respectively, and the exponents of the radial density distributions of these two grain species are set to be equal and denoted as  $p$ . The ranges of the changes of these parameters are as follows:  $\tau_V^{\text{sil}} = 15 \dots 35$  with  $\Delta\tau_V^{\text{sil}} = 5$ ,  $\tau_V^{\text{SIL}} = 1 \dots 3$  with  $\Delta\tau_V^{\text{SIL}} = 0.5$ ,  $r_{\text{in}} = 10 \dots 25 R_\star$  with  $\Delta r_{\text{in}} = 5 R_\star$ ,  $\Theta = 10^\circ \dots 90^\circ$  with  $\Delta\Theta = 20^\circ$ , and  $p = 1.4, 1.6, 1.8, 2.0$ . The outer radius of the disk is set to  $500 \times r_{\text{in}}$ .

Figure 7 shows the best-fit model consisting of small and large silicate grains. The optical depths of small and large silicate grains are  $25 \pm 5$  and  $2.0 \pm 0.5$ , respectively. These optical

depths correspond to 1.9 and 2.5 at  $10 \mu\text{m}$ , respectively. The disk has an inner boundary radius of  $15 \pm 3 R_\star$  and a half-opening angle of  $30^\circ \pm 10^\circ$  with  $p = 1.8 \pm 0.1$ . The inclination angle is derived to be  $45^\circ \pm 10^\circ$ . Figures 7a and 7b illustrate that this model can approximately reproduce the whole SED as well as the silicate emission spectrum, although the predicted silicate emission feature appears too broad compared to the observed spectra. A decrease of the optical depth of large silicate grains can provide a better match to the observed spectra, but the  $N$ -band visibilities predicted by such models do not show the increase from 8 to  $10 \mu\text{m}$  as observed. Figures 7c and 7e–g demonstrate that the  $N$ -band visibilities predicted for the baseline vector perpendicular to the symmetry axis of the model intensity distribution are in rough agreement with the MIDI observations (thin and thick solid lines), although the model visibilities are still somewhat too flat compared to those observed. It should be noted here that the intensity distribution of the large silicate component is more extended than that of the small silicate component, because the former component shows much more scattered light even in the  $10 \mu\text{m}$  region due to the large grain size. As discussed above, the variation of the flux ratio of these two components with different angular sizes (and different wavelength dependences of the angular sizes) produces visibilities which show a wavelength dependence roughly in agreement with the MIDI observations.

The temperatures of the small and large silicate grains at the disk inner boundary are found to be  $\sim 750$  K and  $\sim 590$  K,

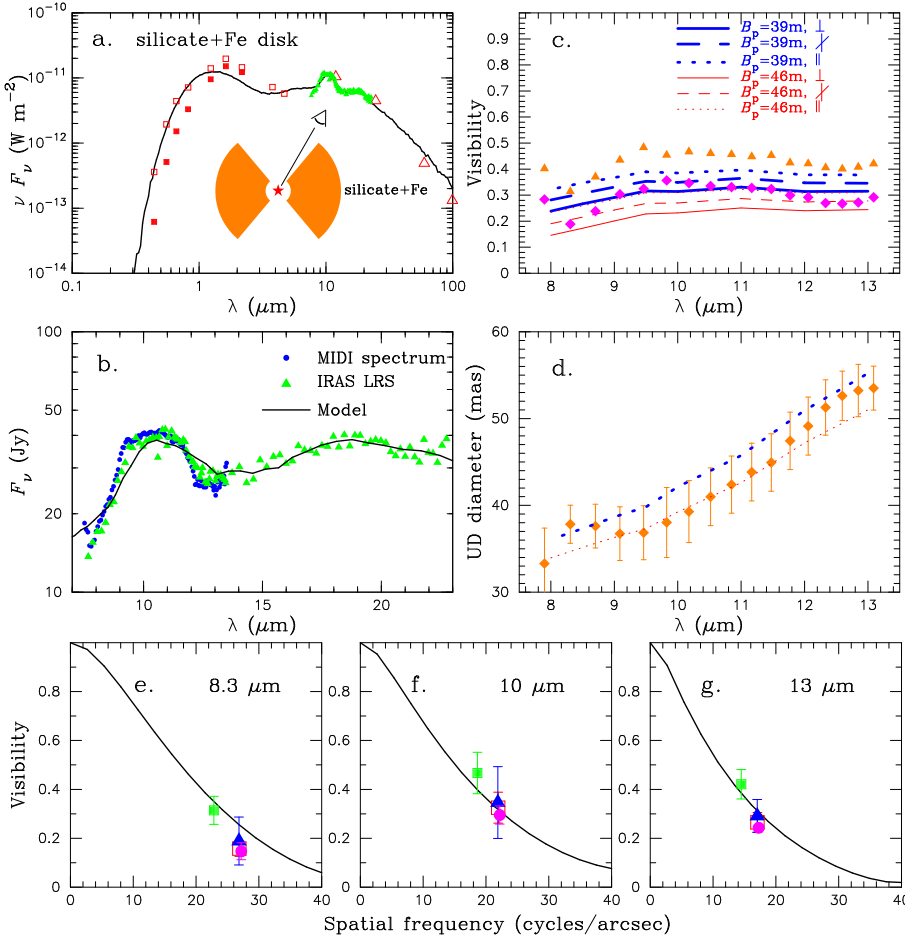


**Fig. 8.** The best-fit disk model consisting of silicate and metallic iron grains (see Sect. 5.3). The parameters of the model are  $\tau_V^{\text{sil}} = 20$ ,  $\tau_V^{\text{Fe}} = 3.0$ ,  $r_{\text{in}} = 20 R_*$  (40 AU),  $p = 1.6$ , and  $\Theta = 50^\circ$ . The model SED and visibilities are calculated for an inclination angle of  $30^\circ$ . See also the legend to Fig. 4 for the references of the symbols. **a.** Comparison between the observed and model SEDs. **b.** Comparison between the observed silicate emission spectra and the predicted spectrum. **c.** Filled triangles and diamonds:  $N$ -band visibilities measured with the 39 m and 46 m baselines, respectively. Thick and thin lines (solid, dashed, and dotted) represent the corresponding model visibilities. See the legend to Fig. 4 for the meanings of the different line types. **d.** The observed uniform-disk diameters are plotted with the filled diamonds. The thick and thin dotted lines represent the uniform-disk diameters predicted for the 39 m and 46 m baselines, respectively, with the baseline vector parallel to the symmetry axis. **e.–g.** The model visibilities predicted with the baseline vector parallel to the symmetry axis are plotted (solid lines) together with the observed visibilities. See Fig. 1 for the references of the symbols.

respectively. The mass of each component is  $8.5 \times 10^{-4} M_\odot$  (small silicate grains) and  $1.8 \times 10^{-3} M_\odot$  (large silicate grains). With a gas-to-dust ratio of 100, the total disk mass is derived to be  $0.3 M_\odot$ . This disk mass is comparable to that derived for the silicate+amorphous carbon model and will be discussed in Sect. 6.

It is worth noting that there is growing observational evidence for the presence of large grains in mass-losing, evolved stars. Jura et al. (2001) conclude that the far-infrared and sub-mm fluxes observed toward the silicate carbon star BM Gem can be explained by grains as large as 0.1 mm. Molster et al. (2001) consider large grains ( $\sim 2 \mu\text{m}$  and  $\sim 300 \mu\text{m}$ ) to explain the mid-infrared spectrum of the silicate carbon star IRAS09425-6040. The lack of the  $10 \mu\text{m}$  silicate feature in this object may even suggest the absence of grains smaller than  $\sim 2 \mu\text{m}$ . The time scale for grain growth by grain-grain collisions (e.g., Jura & Kahane 1999; Yamamura et al. 2000) implies that such large grains can form by coagulation, provided that the disk is stable (see Sect. 6 for discussion on the stability of the disk around silicate carbon stars). The presence of large grains is also inferred in evolved stars other than silicate carbon stars. For example, Jura et al. (1997) surmise that large grains may be responsible for the fluxes at radio wavelengths observed for the post-AGB star Red Rectangle. The radiative transfer modeling of Men'shchikov et al. (2002) for this object also lends support to the existence of grains as large as 0.2 cm. In order to confirm the presence or absence of large grains in

IRAS08002, far-infrared and sub-mm observations would be crucial.

### 5.3. Models with silicate and metallic iron grains

As the third possible scenario, we present models consisting of silicate and metallic iron grains. The model geometry is the same as in the previous subsections (see also the inset of Fig. 8a). The opacity of silicate is calculated from the complex refractive index of the warm silicate of Ossenkopf et al. (1992) for a spherical grain with  $a = 0.1 \mu\text{m}$ . We note that Kemper et al. (2002) found a satisfactory fit to the observed SED of the OH/IR star OH127.8+0.0 by including the opacity of non-spherical metallic iron grains, which were represented with a continuous distribution of ellipsoids (CDE, Bohren & Huffman 1983). Kemper et al. (2002) demonstrate that the opacities of metallic iron calculated in the Mie theory for a spherical grain and with CDE show a substantial difference. They also found that the amount of iron obtained from their modeling with non-spherical iron grains is consistent with the average interstellar abundances of Fe and Si, while the use of spherical iron grains results in a noticeable overabundance of Fe. Therefore, for metallic iron, we use the opacity calculated with CDE using the complex refractive index of Ordal et al. (1988). We denote the optical depths of silicate and metallic iron grains as  $\tau_V^{\text{sil}}$  and  $\tau_V^{\text{Fe}}$ , respectively, and the exponents of the radial density distri-



butions of both grain species are set to be equal and denoted as  $p$ . A grid of models is calculated for the following ranges of the parameters:  $\tau_{\text{V}}^{\text{sil}} = 15 \dots 35$  with  $\Delta\tau_{\text{V}}^{\text{sil}} = 5$ ,  $\tau_{\text{V}}^{\text{Fe}} = 1 \dots 5$  with  $\Delta\tau_{\text{V}}^{\text{Fe}} = 1$ ,  $r_{\text{in}} = 10 \dots 30 R_{\star}$  with  $\Delta r_{\text{in}} = 5 R_{\star}$ ,  $\Theta = 10^{\circ} \dots 90^{\circ}$  with  $\Delta\Theta = 20^{\circ}$ , and  $p = 1.4, 1.6, 1.8, 2.0$ . The outer radius of the disk is set to  $500 \times r_{\text{in}}$ .

Figure 8 shows the best-fit model in this geometry. The optical depths of silicate and iron dust are found to be  $20 \pm 5$  and  $3 \pm 1$  in the optical, respectively, which correspond to  $10 \mu\text{m}$  optical depths of 1.5 and 0.34, respectively. The disk has a half-opening angle of  $50^{\circ} \pm 10^{\circ}$  and an inner boundary radius of  $20 \pm 5 R_{\star}$ , where the temperatures of silicate and iron grains reach  $\sim 620$  K, with  $p = 1.6 \pm 0.1$ . The inclination angle is derived to be  $30^{\circ} \pm 10^{\circ}$ . Figure 8a shows that the observed SED is fairly reproduced by the model, although the model predicts the near-infrared flux to be slightly lower than the observations. This discrepancy may be due to the uncertainty of the effective temperature of the central star as well as the simplifications adopted in our model such as the simple disk geometry with two grain species completely coexisting. Figures 8c and 8e–g reveal that the wavelength dependence of the  $N$ -band visibilities predicted by this model is also in fair agreement with the MIDI observations. In particular, the visibilities predicted for the baseline vector parallel to the symmetry axis of the disk (thick and thin dotted lines) can roughly reproduce the observed visibilities. However, the predicted visibilities are again somewhat too flat between 8 and  $10 \mu\text{m}$  compared to those observed, as in the cases of the two models presented above. The intensity distributions of the silicate and metallic iron components show different wavelength dependences, and the flux contributions of these two components also vary in the  $N$  band. As in the cases of the silicate+amorphous carbon and small+large silicate grain models, the combination of these factors results in a wavelength dependence of the  $N$ -band visibility totally different from that predicted by the models with silicate dust alone.

The masses of silicate and metallic iron dust are derived to be  $4.2 \times 10^{-3} M_{\odot}$  and  $3.9 \times 10^{-4} M_{\odot}$ , with bulk densities of  $3.7 \text{ g cm}^{-3}$  and  $7.9 \text{ g cm}^{-3}$  assumed for silicate and metallic iron, respectively. The mass fraction of metallic iron is about 9%, which is of the same order as the value 4% derived by Kemper et al. (2002) for OH127.8+0.0. As they mention, such mass fractions of metallic iron are consistent with the standard interstellar abundances of Fe and Si, which is not the case for models using spherical metallic iron grains. In fact, we also calculated models consisting of silicate and spherical metallic iron grains with  $a = 0.1 \mu\text{m}$  and found a parameter set that can fairly reproduce the observed SED and  $N$ -band visibilities. However, the mass of metallic iron grains predicted by such a model is comparable to that of silicate dust (a mass fraction of metallic iron dust as high as  $\sim 30\%$ ) and, therefore, cannot easily be explained unless a remarkable overabundance of Fe is assumed as discussed in Kemper et al. (2002) and Harwit et al. (2001).

## 6. Discussion

While we assumed a dust disk surrounding the carbon-rich AGB star (and also its putative low-luminosity companion) in

our models, it is still controversial how oxygen-rich material is stored around silicate carbon stars. Based on the ISO observation of the silicate carbon star V778 Cyg, Yamamura et al. (2000) point out that such a circumbinary disk is exposed to direct radiation pressure from the central star with a luminosity of  $\sim 10^4 L_{\odot}$  and that the disk cannot exist for a long time. They suggest that the oxygen-rich material is stored in the circumstellar disk around a companion, instead of a circumbinary disk, and that the silicate emission originates in the outflow from the circum-companion disk (see Fig. 5 in Yamamura et al. 2000). It should be noted here, however, that the infrared excess of V778 Cyg is much smaller than that of IRAS08002. The silicate emission originating in the outflow from the circum-companion disk would not be sufficient to account for the infrared excess observed toward IRAS08002, because the solid angle subtended by such an outflow would not be very large, and consequently, the amount of dust in the outflow would be small. The infrared excess expected from this scenario may be sufficient to explain the observed infrared excess of V778 Cyg, but possibly not that of IRAS08002.

Also, the optical depths of the disk in our models are significantly larger than that observed in V778 Cyg. Yamamura et al. (2000) stress that the silicate emission is optically thin, and the spherical shell modeling of Kwok & Chan (1993) also suggests that the optical depth of silicate grains in V778 Cyg is  $\sim 0.1$  at  $10 \mu\text{m}$ , which is significantly smaller than the 1.5–1.9 that we derived for IRAS08002. In an optically thin case as in V778 Cyg, radiation pressure is likely to prevent a circumbinary disk from existing for an extended period of time. However, Yamamura et al. (2000) also point out that this may not be the case for objects with optically thick disks such as the Red Rectangle and possibly the silicate carbon star IRAS09425-6040 with high crystallinity and that such optically thick disks can form around close binaries. In those optically thick cases, radiation pressure from the central primary star acts only on the inner surface of the disk and the rest of the disk can be shielded from direct radiation pressure. The stability of such optically thick disks may also provide an environment favorable for grains to grow in large sizes. Therefore, the results of our modeling for IRAS08002 are qualitatively consistent with the stability of the circumbinary disk. Furthermore, the total dust masses derived for our models are of the order of  $10^{-3} M_{\odot}$  and remarkably larger than those derived for V778 Cyg ( $2\text{--}10 \times 10^{-6} M_{\odot}$  by Yamamura et al. 2000,  $2 \times 10^{-7} M_{\odot}$  by Szczerba et al. 2005), but close to the dust mass around IRAS09425-6040 ( $\sim 2 \times 10^{-3} M_{\odot}$ ) derived by Molster et al. (2001). The density distributions in our models ( $p \approx 1.6\text{--}1.8$ ) are also noticeably flatter than those expected for constant mass outflows. Molster et al. (2001) derived such a flat density gradient to explain the ISO spectrum of IRAS09425-6040. These results imply that IRAS08002 may belong to the class of objects (presumably) possessing a dense dust disk like IRAS09425-6040 and the Red Rectangle.

We also mention that the inner boundary radii of our models are  $\sim 15\text{--}20 R_{\star}$ , which means that the diameter of the inner cavity is  $\sim 30\text{--}40 R_{\star}$ . If IRAS08002 is a binary consisting of a carbon-rich primary and a low-luminosity companion, the separation cannot be larger than the diameter of the inner cavity

and is estimated to smaller than  $\sim 30 R_\star$  ( $\sim 60$  AU). This is in contrast with the separation between the binary components in the V778 Cyg system ( $\geq 75$  AU) estimated by Szczerba et al. (2005). Therefore, while such constraints are still rather weak, these results are at least qualitatively consistent with the scenario where a circumbinary disk may form in a close binary system and a circum-companion disk in a wide binary.

We note that the silicate carbon star IRAS04496-6958 discovered in the Large Magellanic Cloud by Trams et al. (1999) exhibits a broad  $10 \mu\text{m}$  spectrum similar to that of IRAS08002. Trams et al. (1999) suspect that the spectrum of IRAS04496-6958 may be explained by silicate and a second grain species such as large silicate grains, silicon carbide (SiC), crystalline olivines, and corundum. As we mentioned in Sect. 5, we did not consider crystalline olivines as the second grain species, because it is not (yet) identified in IRAS08002. We also calculated disk models with SiC or corundum as the second grain species, using the same geometry where silicate and the second grain species coexist everywhere in the disk. However, as far as such a geometry is used, we could not find a model which reasonably reproduces the observed SED and  $N$ -band visibilities, because these models tend to show too strong features due to corundum (at  $\sim 11\text{--}15 \mu\text{m}$ ) or SiC (at  $\sim 11.3 \mu\text{m}$ ). Therefore, corundum or SiC may be present in the circumstellar environment of IRAS08002 as minor dust components, but probably not as major components responsible for the unexpected wavelength dependence of the  $N$ -band visibilities.

There are still discrepancies between the observations and the models. In particular, all three models presented above show the same problem: the predicted  $N$ -band visibilities are too flat between 8 and  $10 \mu\text{m}$ , compared to the MIDI observations. This discrepancy may be attributed to the assumptions used in our models, such as the rather simple disk geometry and the simplified representation of the dust properties. Since the disk geometries considered in the present work are obviously quite simplified, more complicated disk geometries may at least partially explain the discrepancy between the observations and model predictions. An alternative explanation for this systematic discrepancy would be to assume that different grain species have different spatial distributions, instead of co-existing everywhere in the disk. It is plausible that distinct regions of the disk may be predominantly populated with different grain species due to the grain formation and growth processes. However, more observational constraints obtained by complementary observations would be needed to explore such complicated geometries and spatial variations of dust chemistry.

## 7. Concluding remarks

Our MIDI observations of IRAS08002 have resolved the dusty environment of a silicate carbon star for the first time. The observed visibilities show a monotonic increase from 8 to  $\sim 9.5 \mu\text{m}$ , while they remain approximately constant longward of  $10 \mu\text{m}$ . Although axisymmetric disk models consisting of silicate dust alone can reproduce the observed SED reasonably well, they fail to explain the observed  $N$ -band visibilities. This demonstrates the power of spectro-interferometry for probing

the circumstellar environment of objects with a complex geometry and intricate dust chemistry.

We then considered models with silicate and a second grain species, for which we adopted amorphous carbon, large silicate grains, and metallic iron grains. We have shown that such disk models can fairly reproduce the observed SED and  $N$ -band visibilities. The dust disk around IRAS08002 is optically thick in all these models ( $\tau_V^{\text{sil}} = 20\text{--}25$ ) with inner radii of  $15\text{--}20 R_\star$  and half-opening angles of  $30^\circ\text{--}50^\circ$ . The derived density distributions ( $\rho \propto r^{-1.6}, r^{-1.8}$ ) are flatter than those expected for constant outflows. These results are qualitatively consistent with the scenario in which a dense circumbinary dust disk forms in some silicate carbon stars, possibly with a close companion. However, the wavelength dependence of the  $N$ -band visibilities predicted by these models is still somewhat too flat between 8 and  $10 \mu\text{m}$ , as compared to the MIDI observations. It should also be noted that given the simplifications used in the models as well as the lack of complementary observational constraints, the two-grain-species models should be regarded as one of the possible scenarios to explain the unexpected  $N$ -band visibilities of IRAS08002 revealed with MIDI.

Our MIDI observations of IRAS08002 and radiative transfer modeling have revealed that the silicate carbon star puzzle is even more puzzling than previously thought. Mid-infrared interferometric observations with shorter baselines and a wider coverage of position angles would be indispensable for probing the geometry of the dust disk. In order to investigate detailed dust chemistry, high-resolution mid-infrared spectroscopy would be crucial. Far-infrared and sub-mm observations would also be useful for detecting the presence or absence of large grains.

*Acknowledgements.* The authors would like to thank T. Kozasa and I. Yamamura for valuable comments and discussions on silicate carbon stars as well as on dust formation in AGB stars. We are indebted to D. Vinković and A. B. Men'shchikov for fruitful discussions about radiative transfer calculations. We also acknowledge D. Engels for providing us with the results of the VLBA observations before publication.

## References

- Abia, C., & Isern, J. 2000, *ApJ*, 536, 438
- Barnbaum, C., Kastner, J. H., Morris, M., & Likkell, L. 1991, *A&A*, 251, 79
- Benson, P. J., & Little-Marein, I. R. 1987, *ApJ*, 316, L37
- Bergeat, J., Knapik, A., & Rutily, B. 2002, *A&A*, 390, 967
- Bjorkman, J., & Wood, K. 2001, *ApJ*, 554, 615
- Bohren, C. F., & Huffman, D. R. 1983, *Absorption and Scattering of Light by Small Particles*, Wiley, New York
- Chan, S. J. 1993, *AJ*, 106, 2126
- Chan, S. J., & Kwok, S. 1991, *ApJ*, 383, 837
- Chesneau, O., Meilland, A., Rivinius, T., et al. 2005a, *A&A*, 435, 275
- Chesneau, O., Verhoelst, T., Lopez, B., et al. 2005b, *A&A*, 435, 563
- Cohen, M., Walker, R. G., Carter, B., et al. 1999, *AJ*, 117, 1864
- Deguchi, S., Nakada, Y., Sahai, R. 1990, *A&A*, 230, 339
- Engels, D. 1994, *A&A*, 285, 497
- Engels, D., & Leinert, Ch. 1994, *A&A*, 282, 858
- Gail, H.-P., & Sedlmayr, E. 1999, *A&A*, 347, 594
- Groenewegen, M. A. T. 1995, *A&A*, 293, 463



- Groenewegen, M. A. T., Whitelock, P. A., Smith, C. H., & Kerschbaum, F. 1998, *MNRAS*, 293, 18
- Harwit, M., Malfait, K., Decin, L., et al. 2001, *ApJ*, 557, 844
- Ivezić, Ž., & Elitzur, M. 1997, *MNRAS*, 287, 799
- Izumiura, H. 2003, *Ap&SS*, 283, 189
- Jaffe, W. 2004, *SPIE Proc.*, 5491, p.715
- Jura, M., & Kahane, C. 1999, *ApJ*, 521, 302
- Jura, M., Turner, J., & Balm, S. P. 1997, *ApJ*, 474, 741
- Jura, M., Webb, R. A., & Kahane, C. 2001, *ApJ*, 550, L71
- Kahane, C., Barnbaum, C., Uchida, K., Balm, S. P., & Jura, M. 1998, *ApJ*, 500, 466
- Kemper, F., de Koter, A., Waters, L. B. F. M., Bouwman, J., & Tielens, A. G. G. M. 2002, *A&A*, 384, 585
- Kwok, S., & Chan, S. J. 1993, *AJ*, 106, 2140
- Lambert, D. L., Smith, V. V., & Hinkle, K. H. 1990, *AJ*, 99, 1612
- Le Bertre, T., Deguchi, S., & Nakada, Y. 1990, *A&A*, 235, L5
- Leinert, Ch., van Boekel, R., Waters, L. B. F. M., et al. 2004, *A&A*, 423, 537
- Little-Marenin, I. R. 1986, *ApJ*, 307, L15
- Little-Marenin, I. R., Benson, P. J., & Little, S. J. 1987, In: *Cool Stars, Stellar Systems, and the Sun*, eds. J. L. Linsky & R. E. Stencel, Springer-Verlag, Berlin, p.396
- Little-Marenin, I. R., Benson, P. J., & Dickinson, D. F. 1988, *ApJ*, 330, 828
- Lloyd-Evans, T. 1990, *MNRAS*, 243, 336
- Lorenz-Martins, S., & Pompeia, L. 2000, *MNRAS*, 315, 856
- Lorenz-Martins, S., de Araújo, F. X., Condina Landaberry, S. J., de Almeida, W. G., & de Nader R. V. 2001, *A&A*, 367, 189
- Lucy, L. 1999, *A&A*, 344, 282
- Men'shchikov, A. B., Schertl, D., Tuthill, P. G., Weigelt, G., & Yungelson, L. R. 2002, *A&A*, 393, 867
- Molster, F., Yamamura, I., Waters, L. B. F. M., et al. 1999, *Nature*, 401, 563
- Molster, F., Yamamura, I., Waters, L. B. F. M., et al. 2001, *A&A*, 366, 923
- Morris, M. 1987, *PASP*, 99, 1115
- Nakada, Y., Izumiura, H., Onaka, T., et al. 1987, *ApJ*, 323, L77
- Nakada, Y., Deguchi, S., & Forster, J. R. 1988, *A&A*, 193, L13
- Neckel, Th., & Klare, G. 1980, *A&AS*, 42, 251
- Niccolini, G., Woitke, P., & Lopez, B. 2003, *A&A*, 399, 703
- Ohnaka, K., & Tsuji, T. 1999, *A&A*, 345, 233
- Ohnaka, K., Bergeat, J., Driebe, T., et al. 2005, *A&A*, 429, 1057
- Ordal, M. A., Bell, R. J., Alexander, R. W., Newquist, L. A., & Query, M. R. 1988, *Appl. Opt.*, 27, 1203
- Ossenkopf, V., Henning, Th., & Mathis, J. S. 1992, *A&A*, 261, 567
- Pascucci, I., Wolf, S., Steinacker, J., et al. 2004, *A&A*, 417, 793
- Przygodda, F., Chesneau, O., Graser, U., Leinert, Ch., & Morel, S. 2003, *Ap&SS*, 286, 85
- Rouleau, F., & Martin, P. G. 1991, *ApJ*, 377, 526
- Savage, B. D., & Mathis, J. S. 1979, *ARA&A*, 17, 73
- Skinner, C. J., Griffin, I., & Whitmore, B. 1990, *MNRAS*, 243, 78
- Stephenson, C. B. 1973, *A General Catalogue of Cool Carbon Stars*, (Publ. Warner and Swasey Obs., 1, No. 4) (GCCCS)
- Stephenson, C. B. 1989, *A General Catalogue of Cool Galactic Carbon Stars*, Second Ed. (Publ. Warner and Swasey Obs., 3, No. 2) (GCCGCS)
- Suh, K.-W. 2004, *ApJ*, 615, 485
- Szczerba, R., Szymczak, M., Babkovskaia, N., et al. 2005, *A&A*, submitted, also available at <http://xxx.lanl.gov/abs/astro-ph/0504354>
- Trams, N. R., van Loon, J. Th., Zijlstra, A. A., et al. 1999, *A&A*, 344, L17
- Willems, F., & de Jong, T. 1986, *ApJ*, 309, L39
- Wolf, S. 2003, *ApJ*, 582, 859
- Wolf, S., Henning, Th., & Stecklum, B. 1999, *A&A*, 349, 839
- Yamamura, I., Dominik, C., de Jong, T., Waters, L. B. F. M., & Molster, F. J. 2000, *A&A*, 363, 629